Fatigue and Fracture Behaviour of Laser Powder Bed Fusion Stainless Steel 316L: Influence of Processing Parameters

Meng Zhang [a, b], Chen-Nan Sun [c], Xiang Zhang [d], Phoi Chin Goh [b], Jun Wei [c], David Hardacre [b], Hua Li [a*]

[a] *Singapore Centre for 3D Printing, School of Mechanical and Aerospace Engineering, Nanyang Technological University, 50 Nanyang Avenue, Singapore 639798*

[b] *Lloyd's Register Global Technology Centre, 1 Fusionopolis Place, #09-11 Galaxis, Singapore 13852*

[c] *Singapore Institute of Manufacturing Technology, 73 Nanyang Drive, Singapore 637662*

[d] *Faculty of Engineering & Computing, Coventry University, Coventry CV1 5FB, UK*

Abstract

The laser powder bed fusion (L-PBF) process involves a large number of processing parameters. Extending the intricate relationship between processing and structure to mechanical performance is essential for structural L-PBF materials. The high cycle fatigue properties of L-PBF parts are very sensitive to process-induced porosities which promote premature failure through the crack initiation mechanisms. Results from this work show that for stainless steel 316L, porosity does not impinge on the high cycle fatigue properties when processing is kept within a ±30% tolerance band. In this 'optimum' processing region, crack initiation takes place due to defects at the solidification microstructure level. Beyond the 'optimum' processing region, over-melting and under-melting can lead to porosity-driven cracking and inferior fatigue resistance. In addition, regardless of the processing condition, fatigue resistance was found to follow a direct linear relationship with ductility and tensile strength in the low and high stress fatigue regimes respectively.

Keywords: Selective laser melting, laser powder bed fusion, stainless steel 316L, porosity, fatigue property, process window

1. Introduction

* Corresponding author. Email: lihua@ntu.edu.sg

Additive manufacturing (AM) technology offers many benefits over conventional manufacturing methods such as design flexibility and efficient utilisation of resources. However, the forming principles of AM is different from the subtractive techniques. The microstructure and mechanical behaviours of AM materials need to be evaluated for the adoption of this technology for structural applications.

The laser powder bed fusion (L-PBF) is a popular AM technique used for the fabrication of metal components. The fatigue behaviours of L-PBF materials have raised much concern as the fusing of metal powders by a high power laser makes the process prone to forming various types of porosity. Small spherical gas pores are nearly unavoidable as they are present in the powder feedstock. Large irregular defects could be attributed to sub-optimal processing parameter settings which can cause either under-melting or over-melting. In the former case, lack of fusion and balling defects [1, 2] can be formed, whereas in the latter case, keyhole pores [3] and spatter particles [4] are often observed. Under cyclic loading, these pores create local stress concentration and trigger fatigue crack initiation. Results from existing studies highlighted the influence of defects, such as porosity and surface roughness, as the cause for the premature fatigue failure of L-PBF parts [5-8]. Fatigue fracture surface analyses often reveal surface or subsurface pores at crack origins [6, 7, 9-12]. As current L-PBF systems favour the building of small parts, for which fatigue crack initiation occupies a significant portion of the total life, porosity plays a critical role on the fatigue performance of L-PBF components.

As the L-PBF technology matures and users' familiarisation with the process increases, better control of porosity can be achieved such that fatigue studies should take into consideration the competing effect of both porosity and microstructure. The rapid cooling process is known to generate unique solidification microstructures. The ultrafine grains are in the order of a few microns [13, 14], which is much smaller than the length scale of casting where dendrite cells and second phase particles are in the order of tens of microns [15, 16]. This gives rise to the superior tensile strength of L-PBF materials [17]. In terms of the impact on cyclic properties, ultrafine grains, e.g. produced by equal-channel angular pressing, are effective at creating retarding effects on dislocation movement and crack initiation [18, 19]. The fatigue damage mechanism of ultrafine-grained austenitic materials was studied by Hamada *et al*. [20], where the nucleation of fatigue cracks was found to occur at grain boundaries such that

fracture was intergranular in nature. For the coarse-grained counterpart, failure occurred by the transgranular path due to high concentration of strain inside slip bands.

Moreover, as a result of intrinsic material properties, materials have different tolerance towards defects such that the relative importance of porosity and microstructure on fatigue behaviours should be material-specific. For example, unlike Ti6Al4V [21] and CoCr alloy [22], which showed strong defect-oriented fatigue behaviour, i.e. the fatigue strength was markedly improved after hot isostatic pressing (HIP) treatment, stainless steel 316L was found to be highly defect- and residual stress- tolerant such that HIP and stress relieving heat treatments were unable to improve its fatigue strength [23, 24]. As stainless steel 316L has a single phase austenitic structure that is devoid of the brittle martensite phase, its defect-tolerant behaviour is believed to be a result of its high ductility, which reduces the notch sensitivity. Consequently, for stainless steel 316L, efforts have been directed towards studying the influence of the solidification microstructure. Pace *et al.* [25] reported that cyclic loading creates microstructural changes in terms of the migration of Molybdenum elements towards the grain boundary and grain coarsening due to the transformation of metastable austenite phase. Ganesh *et al*. [26] studied the fatigue crack growth properties of stainless steel 316L made by an extrusion-based direct metal deposition (DMD) AM system. Evolution of strain-induced martensites was found at the crack tip. This phase is known to promote the reduction of fatigue crack growth rate.

Applications of stainless steel 316L, e.g. body implants [27, 28] and heat exchangers, often desire good fatigue properties. Since it cannot be modified by post-processing heat treatment, the influence of processing condition becomes more relevant. This work aims to study the process-structure-property relationship of stainless steel 316L by highlighting the possible process-induced fatigue failure mechanisms and drawing quantitative correlations between processing and mechanical properties. Results from this work can provide a guide on the high cycle fatigue failure modes that could be expected for different L-PBF processing regimes.

2. Materials and Experimental Methods

2.1 L-PBF Sample Fabrication

Commercially available stainless steel 316L powder with a predominantly spherical shape (Figure 1 (a)) was used. Samples were prepared by a L-PBF system (EOS M 290) installed with a Yb-fibre laser. Five sets of samples, denoted as $0.5P_0$, $0.7P_0$, P_0, $1.3P_0$ and $1.5P_0$, were fabricated by varying one of the key L-PBF processing parameters – laser power, by 50%, 70%, 100%, 130% and 150% from the optimised setting P_0 respectively. No post-processing heat treatment was conducted. The effect of any difference in residual stress caused by processing on mechanical properties was assumed negligible as fatigue properties of stainless steel 316L are insensitive to residual stress [23, 24]. Also, laser power has the least influence on residual stress in comparison with other L-PBF parameters such as platform preheating temperature, powder layer thickness and scan speed [29]. Besides, cutting test samples from the build platform will release considerable part of the thermal residual stress.

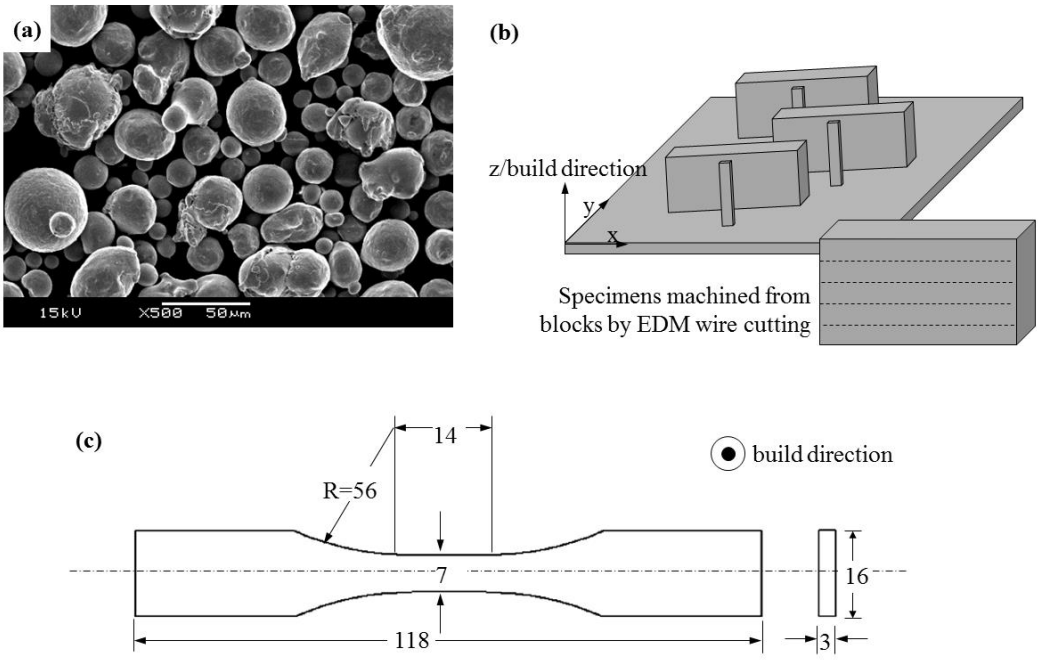

Figure 1 (a) SEM image of the stainless steel 316L powder used in this study, (b) orientation of sample blocks on the build platform and preparation of test specimens by wire cut electrical discharge machining. The x-y plane is referred to as the horizontal plane and planes parallel to the z axis are referred to as the vertical plane in the main text. (c) Geometry of fatigue specimens, dimensions are in mm.

2.2 Porosity and Microstructure Characterisation

Characterisation of microstructural features was done on small test blocks built adjacent to the sample blocks shown in Figure 1 (b). Porosity was measured by the Archimedes method (Mettler Toledo XS204) [30], image analysis of metallographic cross sections and three-dimensionally by the X-ray computed tomography (XCT) technique (Bruker SkyScan 1173). Samples were grinded to remove end of track pores, which could be induced at high laser power due to powder denudation [31], before making any measurements. XCT samples in the form of cuboids with transverse cross sections of approximately 2.5×2.5 mm^2 were scanned at a voltage of 130keV and effective pixel size of 18.5 μm. Etching was done using a solution of 5g $CuCl_2$, 100 mL HCl and 100 mL ethanol.

Pore size was described by the Gumbel extreme value distribution. Proposed by Murakami *et al*. [32, 33], the extreme value distribution is included in the ASTM E2283 for the evaluation of indigenous inclusions due to its strong correlations with component fatigue strength and life. 30 random images each of area A_0=0.31 mm^2 were taken on metallographic planes parallel to the build direction using optical microscope. The equivalent spherical diameter of the pore with the largest area in each image was used as the input for estimating the Gumbel distribution parameters by the maximum likelihood method. The Gumbel cumulative distribution is given by:

$$F(x) = \exp\left(-\exp\left(-\frac{x-\lambda}{\delta}\right)\right)$$

where x is the equivalent spherical diameter, λ and δ are the location and scale parameters of the distribution respectively. For the Gumbel distribution, λ is equal to the mode of the distribution.

2.3 Mechanical Tests

All mechanical tests were conducted on samples with build direction perpendicular to the loading direction as illustrated in Figure 1 (b). The samples were machined by electric discharge machining (EDM) wire cutting into geometry as specified by the ASTM E466 (Figure 1 (c)). Samples were manually grinded before mechanical testing, resulting in a minimum material removal of 20 μm on each surface. This is to remove any near-surface microstructure and residual stress generated by the wire cutting process, which could produce

detrimental effect on fatigue resistance [34]. Two dimensional porosity area fraction as well as hardness measurements were done at six different heights on the test blocks and analysed by the statistical ANOVA method. Results showed no significant change of porosity and hardness with build height at 95% confidence level. Thus, fatigue specimens sliced from the same blocks were assumed to be identical despite being fabricated at different heights from the build platform. Force-controlled fatigue tests were performed under sinusoidal loading at R=0.1 on a servo hydraulic testing system (MTS 810) at a frequency of 5Hz and ambient conditions. A sample that did not fail after 10^6 cycles was considered as a run-out. Tensile tests were conducted on a universal testing machine using the same sample as the fatigue tests. They were tested in displacement control with a crosshead speed of 0.2 mm/min.

3. Results and Discussions

3.1 L-PBF Process Regimes

The process-porosity relationship of the samples was evaluated by using processing information from the literature as the baseline for comparison. As shown in Figure 2, a total of 134 data points, involving five different commercial L-PBF systems, were collected from the literature [30, 35-41]. The key processing parameters, including laser power P, scan speed v, hatch spacing h and powder layer thickness t, were expressed in terms of a unifying parameter, the volumetric energy density E_d ($=P/vht$), which is a thermodynamic term that quantifies the amount of energy reaching the powder bed. A reference volumetric energy density E_{d0} was assigned for describing the process regimes; it was given a value of 100 J/mm^3 as at this volumetric energy density, stainless steel 316L with the least porosity, good surface finish and hardness could be produced [38]. As annotated in Figure 2, these regimes are:

(1) $0.7E_{d0} < E_d < 1.3E_{d0}$ – optimum processing with high relative density close to 99% (grey region);
(2) $0.5E_{d0} < E_d < 0.7E_{d0}$ – inconsistent density; and
(3) $E_d < 0.5E_{d0}$ – drastic reduction in density.

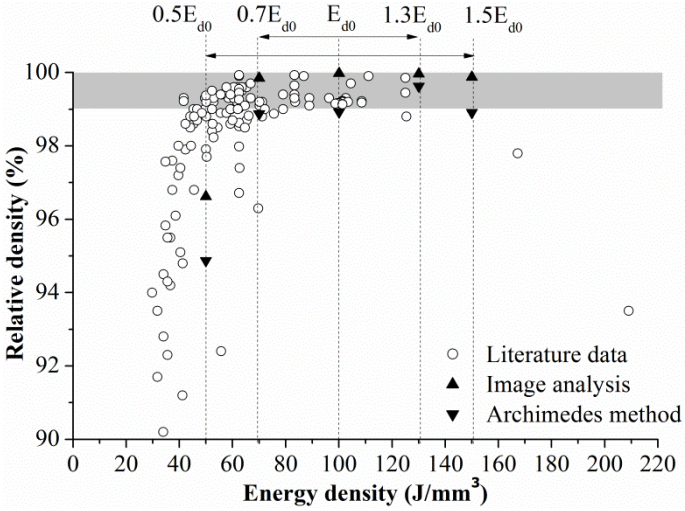

Figure 2 Relative density against volumetric energy density results from the literature [30, 35-41] and the samples used in this work (black triangles) for the processing of stainless steel 316L by laser powder bed fusion.

No clear distinction can be found on the plus E_{d0} side due to the lack of data points in that region. Density results for the current samples are in good agreement with the literature data. The highest densities were found at $1.3P_0$. Reduction in the laser power led to a gradual drop in part density till $0.7P_0$, and a drastic drop at $0.5P_0$. Increasing the laser power from $1.3P_0$ also resulted in a small decrease in the density for $1.5P_0$. Both the image analysis and Archimedes methods produced the same trend with changing energy density, though measurements obtained by the Archimedes method are generally lower.

3.2 Porosity and Micro-cracks

As density measurements only provide a preliminary estimate of the part quality, further porosity characterisation tests were performed. Optical micrographs of the samples are shown in Figure 3. $0.5P_0$ contained large irregular voids, which are lack of fusion defects due to insufficient energy input. Voids in the other samples are mainly small and spherical. Voids in $0.7P_0$ also exhibit characteristics of the lack of fusion defects, i.e. some are triangular in shape and are aligned in the layer direction, which are indicative of insufficient layer-layer or track-track overlapping. Etching confirmed the presence of lack of fusion pores in $0.7P_0$. As shown in Figure 4 (a), an un-melted powder, which retained the original dendritic structure, was found adjacent to a triangular void.

Another type of defect found in the samples is micro-cracks. Large and randomly distributed cracks were present in $1.5P_0$ (Figure 4 (b)). Small amount of cracks were also found in $1.3P_0$. These cracks are likely to be thermal cracks caused by the high laser power. In welding, high heat input decreases the threshold stress for cracking and increases cracking susceptibility [42]. The temperature gradient [43] and residual stress could be too high at $1.5P_0$ that thermally-induced cracks were formed.

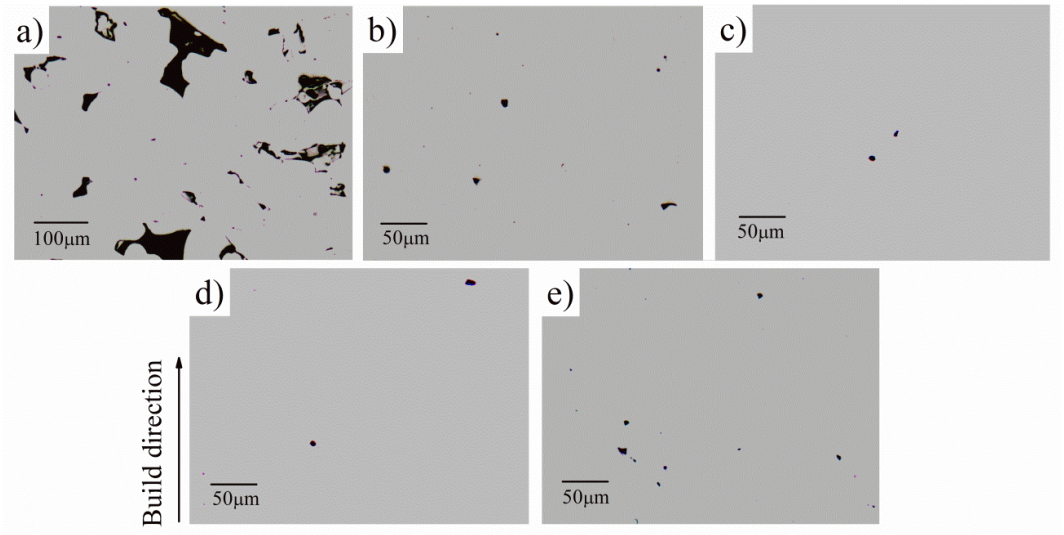

Figure 3 Optical micrographs (a)-(e) of $0.5P_0$, $0.7P_0$, P_0, $1.3P_0$ and $1.5P_0$ respectively. Black regions are pores or cracks.

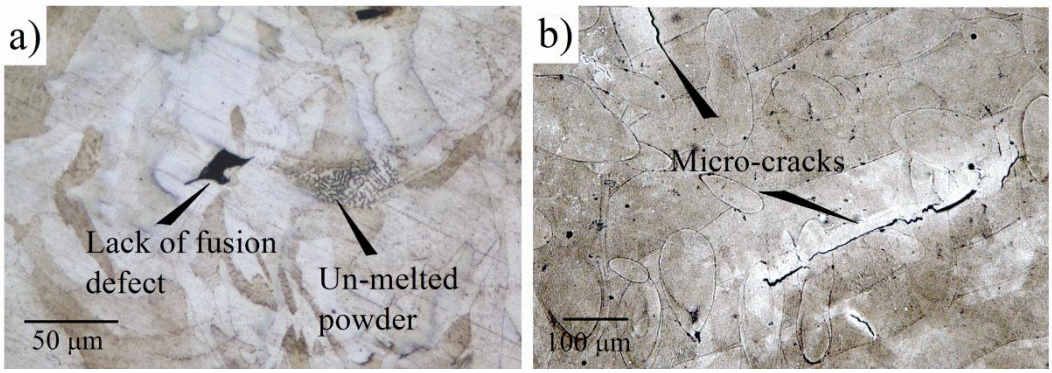

Figure 4 (a) Lack of fusion defects and un-melted powder in $0.7P_0$ (vertical plane) and (b) interconnected cracks in $1.5P_0$ (horizontal plane).

The size distributions of the defects as described by the Gumbel Extreme Value Distribution are shown in Figure 5. The location and scale parameters (λ, δ) in μm are (41.8, 9.6), (10.1, 3.1), (6.6, 4.3), (4.8, 1.7) and (8.7, 4.8) respectively for the samples built with increasing laser

power. Agreeing with the trend in Figure 2, defect size reduces with increasing laser power till $1.3P_0$; at $1.5P_0$, defects are larger but still comparable in size with $0.7P_0$ and P_0. Since the relative density of $1.5P_0$ is lower than P_0, the comparable pore sizes could imply that $1.5P_0$ contained a larger number of pores.

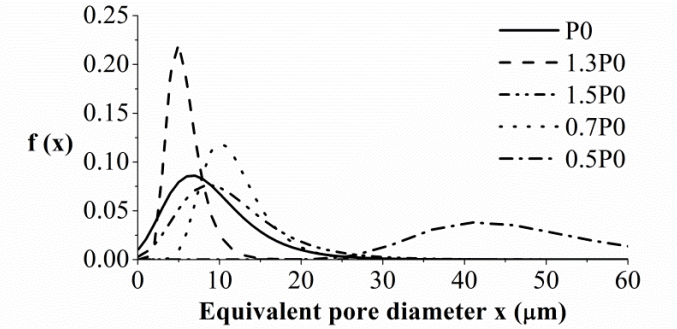

Figure 5 The probability density function f(x) = dF(x)/dx of the Gumbel Extreme Value Distribution of the samples.

XCT reconstruction (Figure 6) revealed larger voids than those captured by the optical microscope. For $0.5P_0$, the largest pore detected by XCT has an equivalent spherical diameter of 340 μm (Figure 6 (a)). This is significantly larger than that described by the Gumbel distribution. This could be attributed to stereological effect, as pores in $0.5P_0$ are irregular in shape and interconnected such that a single large pore could appear as a cluster of closely spaced but individual pores on a two dimensional cross section. Analysis done based on images captured by the optical microscope will lead to underestimation of the actual pore size. For the near fully dense samples, i.e. $0.7P_0$–$1.5P_0$, intermittent large pores were detected as XCT allowed a larger volume to be inspected. The largest pore detected in $0.7P_0$ is about 100 μm (Figure 6 (b)), while the largest pore in $1.5P_0$ is about 65 μm. For P_0 and $1.3P_0$, the largest pores are about 40 μm. These pores could be formed as a result of large contaminants being present in the powder feedstock due to powder reuse.

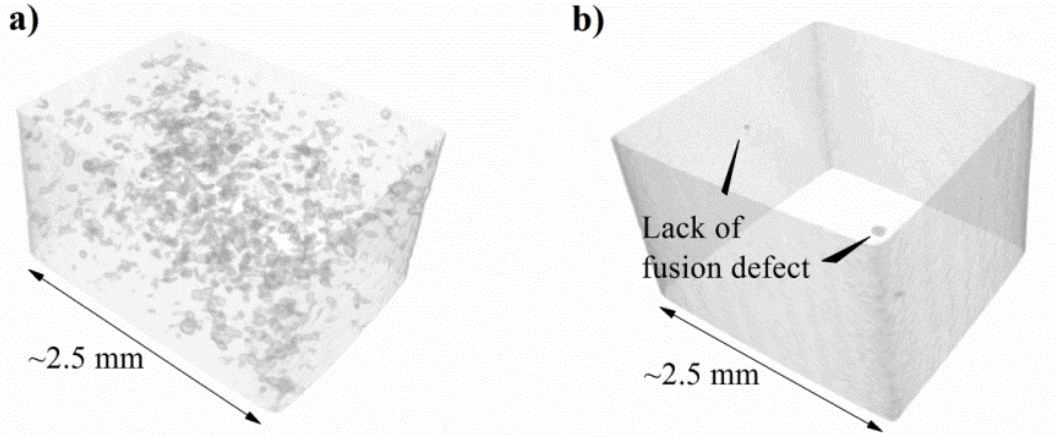

Figure 6 XCT reconstruction of (a) $0.5P_0$, showing extensive interconnected lack of fusion defects and (b) $0.7P_0$, showing intermittent lack of fusion defects.

The observed porosity can be correlated to the processing conditions. The small spherical defects found in the samples were likely to be caused by entrapped gas in the raw stainless steel 316L powder and ambient gas from the build chamber [44]. The steep temperature gradient during the L-PBF process gave rise to rapid cooling and prevented the entrapped gas from escaping the melt pool. Such pores were present in all samples regardless of the processing condition. Increasing the laser power, however, could have facilitated the diffusion of the entrapped gas from the melt pool as materials were held at a higher temperature for a longer time. Also, the higher energy input could have produced a more flattened melt pool [36], which reduced the travelling distance of the entrapped gas. This explains why pores in $1.3P_0$ are smaller than P_0. Further increase in the laser power, i.e. $1.5P_0$, caused a reversal of the trend as excessive laser power can lead to powder denudation and mass transfer phenomenon where large spherical defects with ribbed surface can be generated due to the turbulent melt pool [45]. Spatter particles formed at high heat input are usually larger than the metal powder; they cannot be effectively melted by the laser beam and remained as inclusions [4, 46]. Moreover, vaporisation of low melting point contents could have led to the formation of keyhole pores which were deeply embedded in the bulk material [3].

As the processing parameters were optimised at P_0, reducing laser power from P_0 led to smaller melt pools. For $0.7P_0$, the laser power was high enough to allow remelting of the melt pool, but due to inter-layer scan track rotation, poor track-track and layer-layer bonding was possible at the borders of the melt pool where penetration depth was low [47] and thereby

small lack of fusion defects were formed. At $0.5P_0$, the input energy was too low to allow remelting of the adjacent tracks and layers. Lack of fusion defects linked up during the layer-by-layer processing and formed an extensive network of large interconnected pores.

Results from the porosity characterisation tests provided further information on the process regimes identified in Figure 2. At low input energy, the inconsistent density region is characterised by the initial appearance of lack of fusion defects. This processing region should be avoided as it is highly sensitive to process fluctuations which can shift processing into the drastic density reduction region. On the high input energy end, the inconsistent density regime is caused by the turbulent melt pool. Porosity formed in this region are smaller than the lack of fusion defects. However, in this region, parts are prone to forming thermal cracks.

3.3 Monotonic Properties

The monotonic tensile properties of the samples are displayed in Figure 7. An optimum region exists between $0.7P_0$ and $1.3P_0$ for which strength is the highest; strength reduces at both $0.5P_0$ and $1.5P_0$. This is in agreement with the trend observed for the relative density, except that the relative reduction in strength for $0.5P_0$ is less significant. The ductility, in terms of the percentage elongation to failure, shows a different behaviour with the changing processing parameter. The optimum region exists at $0.7P_0$. It reduces with increasing laser power and appears to stabilise at $1.3P_0$.

The inferior strength and ductility of $0.5P_0$ is likely a result of porosity. Conventional porous materials are usually grouped into three categories according to the porosity volume [48]: less than 10%, 10% to 70% and greater than 70%. Samples in this work are in the less than 10% category where the elastic-plastic behaviour vary linearly with porosity [49]. Pre-existing voids increase the strain at the root of the voids and promote crack growth. This is responsible for the poorer monotonic properties of $0.5P_0$. Since ductility generally shows greater change to porosity fraction than tensile strength [50], the larger percentage reduction in the elongation to failure is understandable.

For $1.5P_0$, since pores are similar in size as $0.7P_0$, factors other than porosity could have contributed to its lower strength. Micro-cracks could be one of the factors. Another factor could be the grain size. The strength of L-PBF stainless steel 316L was reported to be very sensitive to the sub-grain size [51]. According to the solidification theory, dendrite cell size is controlled by the cooling rate. In the context of this work, the Rosenthal solution and finite element results indicate that lower laser power generates higher cooling rate [52, 53], and thereby finer dendrite structure. Thus, according to the Hall-Petch equation, the coarser sub-grains in $1.5P_0$ could have contributed to the lower strength.

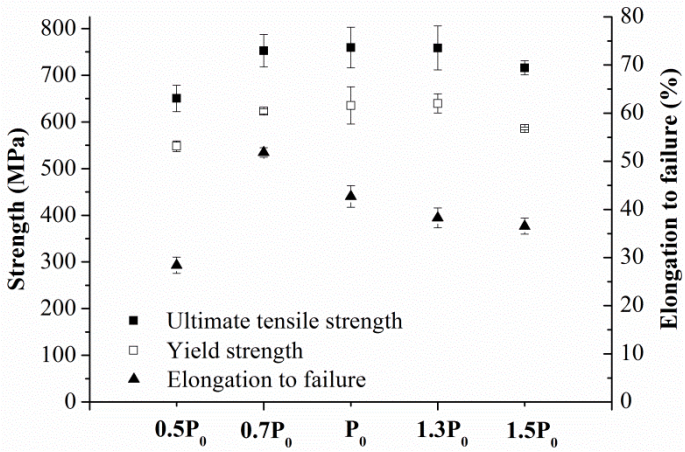

Figure 7 Ultimate tensile strength, 0.2% offset yield strength and percentage elongation to failure of the samples.

For samples from $0.7P_0$ to $1.3P_0$, the elongation to failure reduced despite the reduction in porosity. Other micromechanisms of fracture than porosity could be at play as pores in these parts are too small and sparse to have produced an effect on the macroscopic material failure. Studies on casting have shown that the ductility of solidification structure is dependent on the size of the dendrite cells and second phase particles, and the rate of particle cracking [54]. For finer structures with smaller interdendritic particles, the particles tend to accumulate at grain boundaries, making the dendrite cell boundary more discontinuous, resulting in intergranular grain boundary fracture [15, 16]. For coarser dendrite structures, particles can be closely packed at both the dendrite cell and grain boundaries. Cracking at the particles can extend through the dendrite cells, resulting in transgranular fracture. In the former case, dislocation slipping takes place over a longer distance and produces higher ductility. For L-PBF parts, grain boundary and interdendritic defects could be in the forms of oxide nano-inclusions [13]

and gas porosity. Faster cooling in $0.7P_0$ could have resulted in finer dendrite and particles and the accumulation of these particles at the grain boundary, thereby the higher ductility.

3.4 High Cycle Fatigue Properties

The stress-life (S-N) curves of the samples are shown in Figure 8. Only $0.5P_0$ experienced significant reduction in fatigue strength. The S-N properties of the rest appear to be nearly identical. To further distinguish the fatigue properties of the samples, experimental S-N data obtained at applied cyclic stresses of 438 MPa (low stress) and 657 MPa (high stress) was replotted in Figure 9. The data for $0.5P_0$ at 657 MPa was extrapolated based on a linear S-N relationship. It appears that the fatigue life of the samples varies in a similar manner as the ductility under low stress cyclic loading, whereas it varies similarly as the tensile strength under high stress cyclic loading.

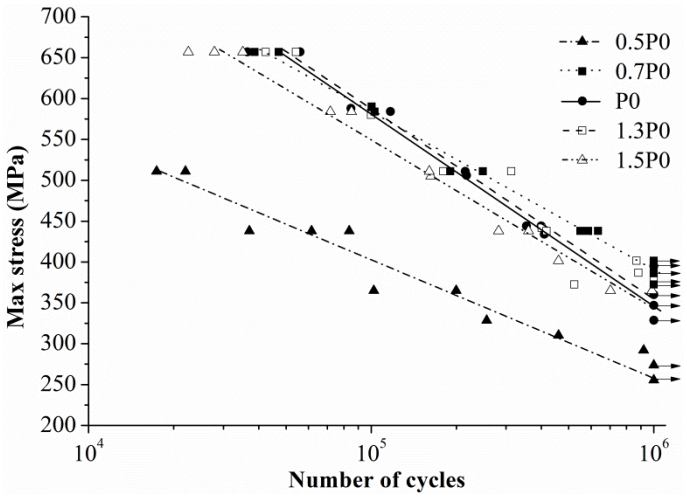

Figure 8 S-N curves of laser powder bed fusion 316L samples made with different laser powers.

To verify the observation, the low stress fatigue life data was plotted against the elongation to failure and the high stress fatigue life data was plotted against the ultimate tensile strength in Figure 10. Fatigue life varies linearly with the respective monotonic tensile parameters. $0.7P_0$, which has the highest ductility, failed after a discernibly larger number of cycles than the rest of the samples under low cyclic stress.

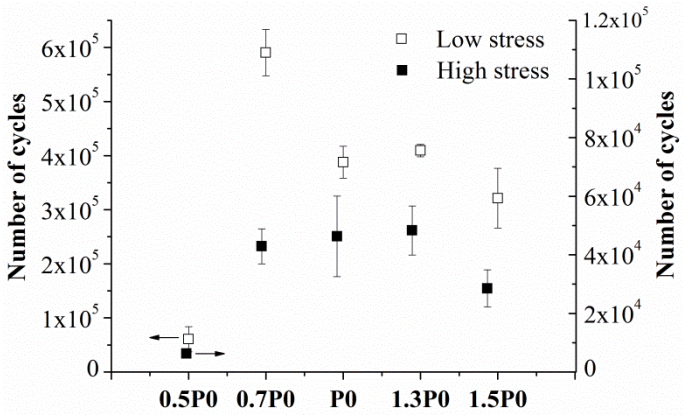

Figure 9 Experimental fatigue life data of the samples subjected to maximum applied cyclic stress of 438 MPa (low stress) and 657 MPa (high stress).

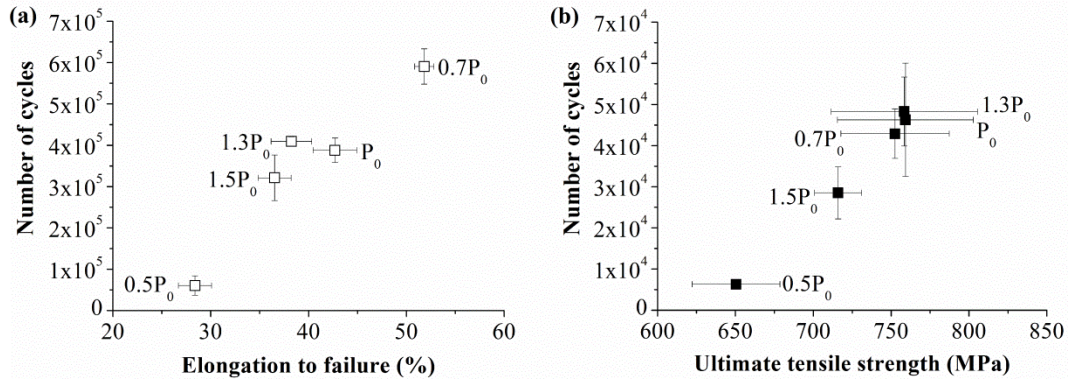

Figure 10 Variation of fatigue life with (a) ductility under low cyclic stress (438 MPa) and (b) ultimate tensile strength under high cyclic stress (675 MPa).

The correlation between fatigue life and tensile strength under high cyclic stress is intuitive as materials with higher monotonic strength could withstand higher cyclic loading as well. However, the correlation with ductility under low cyclic stress is not as straightforward. For conventional materials, ductility is only relevant to the low cycle fatigue condition or to cases of over-loading [55] where materials undergo plastic deformation. To evaluate the fracture mechanism that could have contributed to the observation, fractography analysis was done on fatigue samples that had been subjected to a maximum cyclic stress of 438 MPa, as described in the following sections.

A. Porosity-driven Crack Initiation – $0.5P_0$ and $1.5P_0$

Figure 11 shows the SEM fracture surface of $0.5P_0$ containing a large amount of voids and unmelted powders. Cracks developed at individual voids and joined the main propagation path. By using the S-N curve of P_0 as the reference, a factor of about 12 on life needs to be applied to account for $0.5P_0$. For conventional stainless steel 316L, the initiation and growth of microstructurally small cracks to about 300 μm are responsible for more than 50% of the total life time under cyclic loading (a factor of about 2 on life) [56]. This is comparable with the size of the largest defect in $0.5P_0$ found by XCT. The much larger reduction in fatigue resistance is due to the interaction effect among the defects. For L-PBF, localised heating produced homogenously distributed defects throughout the sample. In this processing regime, not only the size of the pores, but also the number and the distance between the pores are the important influencing factors on fatigue resistance.

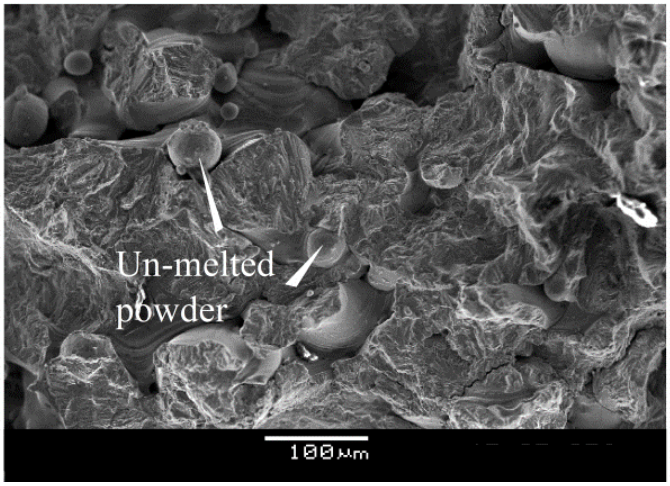

Figure 11 SEM image of the fracture surface of $0.5P_0$ subjected to a maximum cyclic stress of 438 MPa showing a large amount of porosity and un-melted powders.

Figure 12 shows the fractographs of $1.5P_0$. Four major crack origins due to initiation from surface pores, labelled as O1-O4, are visible in Figure 12 (a). The size of the pores at O1 to O3 are about 40 to 50 μm, which are larger than those found by the optical microscope but are within the size of the largest defect detected by XCT. Figure 12 (b) is an enlarged view of the failure site at O2. A rugged morphology was formed due to the linking of the dominant defect (indicated by arrow labelled as 'O2') with a series of smaller defects on both sides of it. The small defects are about 9 μm in size. This shows that even though crack initiation occurred at the larger defect, the small defects are large enough to trigger crack initiation. For such porosity-driven cracking, transgranular propagation took place immediately after the

crack was initiated. Figure 12 (c) shows that the crack origin at O4 is a surface pore about 10 μm. Judging by the surface morphology of the pore and the surrounding material matrix, it could be an interdendritic pore due to gas trapped between adjacent dendrites during rapid solidification. As cooling rate is slower at the higher laser power, pores can grow [57] and become large enough to initiate fatigue cracks.

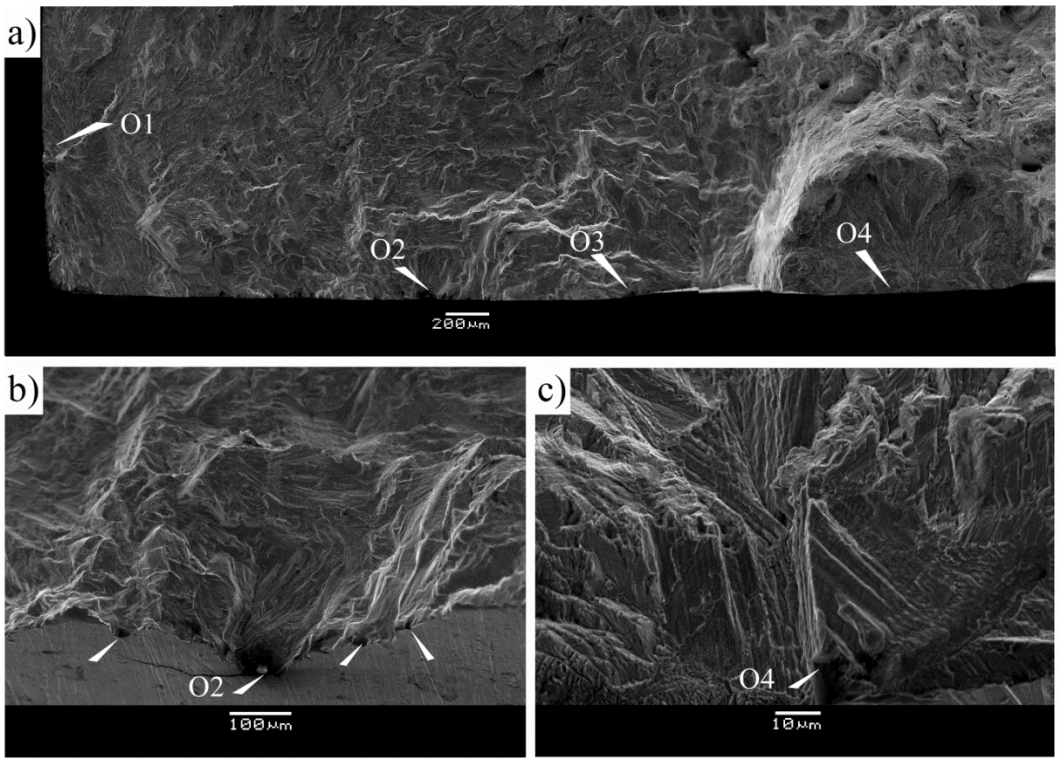

Figure 12 SEM images of fatigue initiation features for 1.5P_0 subjected to a maximum cyclic stress of 438 MPa. (a) Porosity-driven crack initiation sites are labelled as O1-O4, (b) and (c) are the enlarged views of O2 and O4 respectively.

As the global crack propagation direction is from the left to the right of Figure 12 (a), i.e. increasing over-loading due to reduction in load-bearing area over time, the four crack initiation sites provide a ranking of the relative ease of the defects towards crack initiation. Large pores at O1 created the highest stress concentration effect and were the first to crack. The pore at O4 is smaller and took longer time to develop and propagate, and it only joined the main propagation path when the sample had almost reached the unstable crack propagation and final failure phase.

B. Microstructure-driven Crack Initiation - 0.7P_0, P_0 and 1.3P_0

The SEM fracture images of 0.7P_0, P_0 and 1.3P_0 are shown in Figure 13. The dash lines mark the boundary between crack initiation and stable propagation, which is characterised by a faceted crystallographic appearance. The size of the crack initiation region decreases from 0.7P_0 to 1.3P_0. Figure 13 (b), (d) and (f) are the enlarged views of the crack origins for 0.7P_0, P_0 and 1.3P_0 respectively. A mixture of transgranular ('A') and intergranular ('B') features are present. A large area of intergranular fracture at grain boundaries can be seen in 0.7P_0. For P_0 and 1.3P_0, the intergranular fracture regions are much smaller.

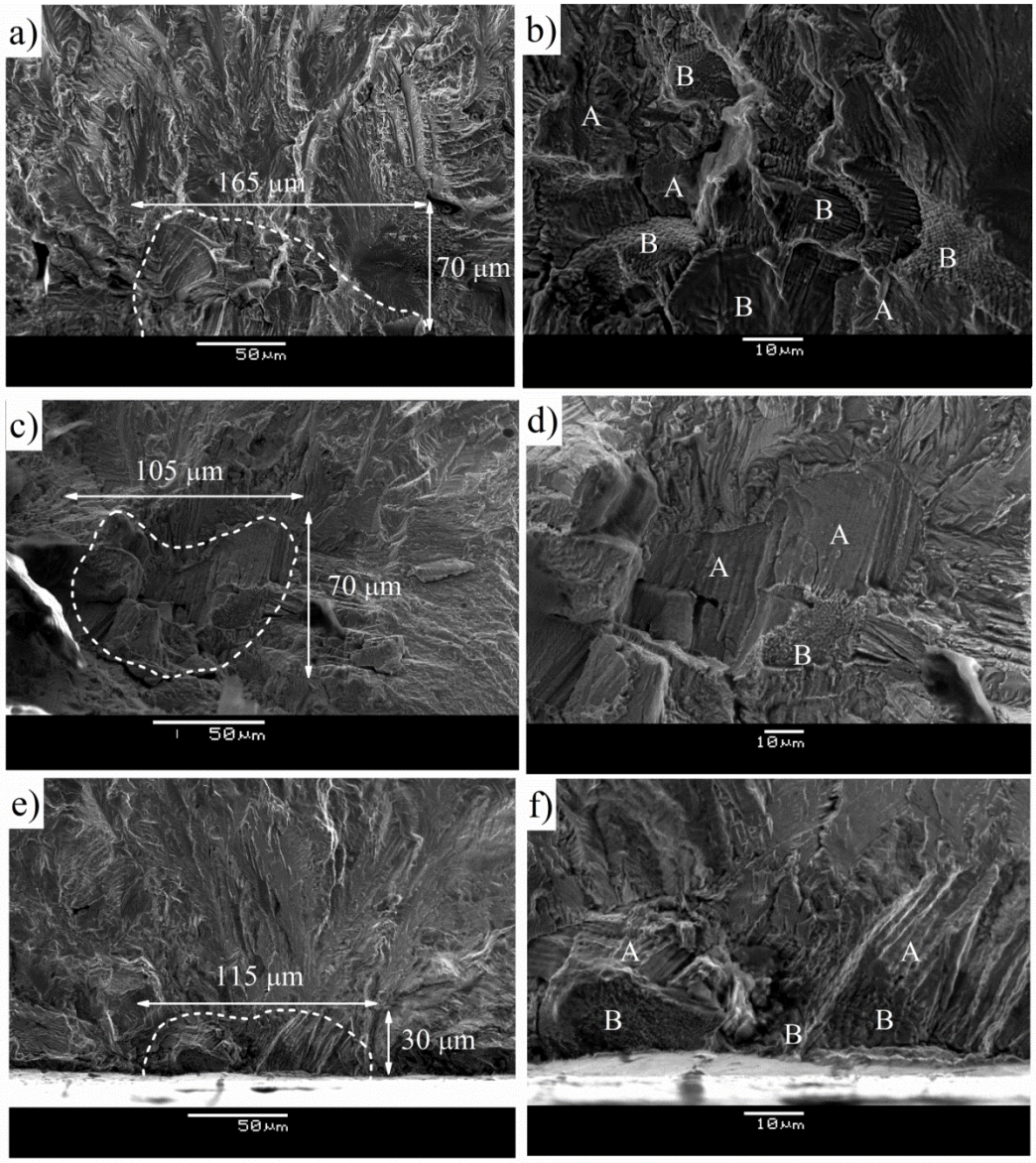

Figure 13 SEM images of fatigue initiation regions for 0.7P_0, P_0 and 1.3P_0 subjected to a maximum cyclic stress of 438 MPa. (a), (c), (e) Crack initiation regions, marked by dash

lines, of $0.7P_0$, P_0 and $1.3P_0$ respectively. (b), (d), (f) Enlarged views of (a), (c), (e) respectively showing mixed transgranular ('A') and intergranular ('B') failure modes.

Figure 14 compares the solidification dendrites at the crack initiation sites of $0.7P_0$ and $1.3P_0$. The image for $1.3P_0$ was taken for a sample loaded at 511 MPa, as at the lower applied stress, intergranular fracture was not as distinct. At the boundary between differently oriented grains, $0.7P_0$ clearly failed by the intergranular route, revealing the dendrite cells. For $1.3P_0$, only parts of the dendrites are discernible at the grain boundary. Failure occurred along the cell boundaries, giving rise to transgranular cracking.

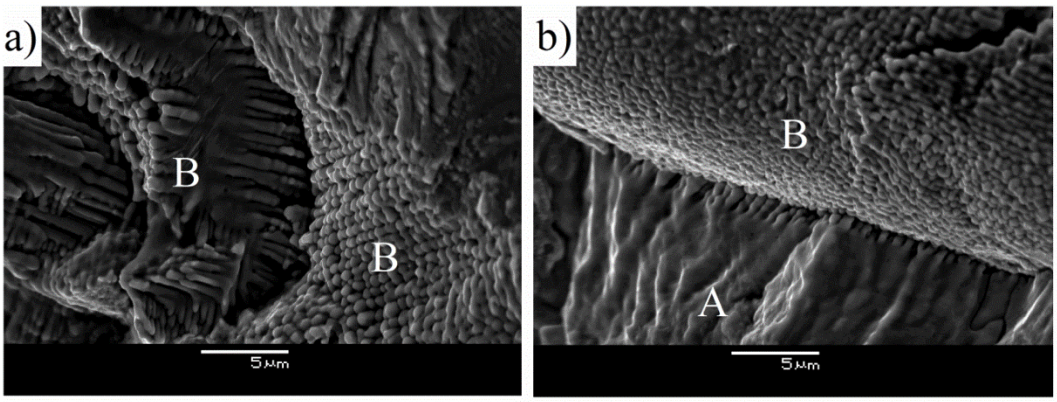

Figure 14 SEM images of dendrite cells in (a) $0.7P_0$ and (b) $1.3P_0$ showing transgranular ('A') and intergranular ('B') fracture modes.

The above observations allude to a strong influence of the solidification microstructure on the fatigue crack initiation mechanisms of $0.7P_0$-$1.3P_0$. This is not surprising as at low cyclic stress, the size of the plastic zone is small such that it is comparable to or even smaller than the local microstructural heterogeneity. Fatigue properties in this region are known to be very sensitive to microstructure.

As explained in section 3.3, cooling rate is affected by the laser power setting. Faster cooling at lower laser power promotes the formation of finer dendrites and second phase particles at grain and dendrite cell boundaries. For L-PBF stainless steel 316L, Saeidi *et al*. [13] reported that the sub-grain boundaries are enriched with dislocations due to misplaced Molybdenum elements. Oxide silicate nano-inclusions were also found, possibly as a result of the absorption of remnant oxygen in the build chamber. In addition, interdendritic pores, which adopt the shape of the surrounding dendrites and are therefore irregular in shape, are also

present. Under remote elastic stress, these discontinuities create local stress concentration. In the case of the nano-inclusions, residual stress can be created during processing as a result of the different thermal expansion coefficients of the silicate and the stainless steel matrix. Fatigue crack initiation can take place at these defects.

Previous experimental works have demonstrated that for cast parts, in the absence of critical defects, fatigue resistance is controlled by the sizes of the dendrite cell and second phase particle [58, 59]. Based on the fractographic observations, the possible fracture mechanisms for the L-PBF samples are illustrated in Figure 15. For $0.7P_0$, dendrites are smaller in size as a result of the more rapid cooling. Particles tend to cluster at grain boundaries rather than dendrite cell boundaries such that the grain boundaries are heavily strained. Particle cracking and the joining of micro-cracks at grain boundaries lead to intergranular fracture. At higher laser power, the coarser dendrites can accommodate more particles. Cracks initiation can now take place at the cell boundaries, leading to transgranular fracture. In reality, cooling rate does not only affect the dendrite cell size, but also the shape and size of the defects. For example, as explained in the case of $1.5P_0$, larger and more irregularly-shaped interdendritic pores could be formed due to slower cooling. They create stronger stress concentration effect and accelerate the cracking process.

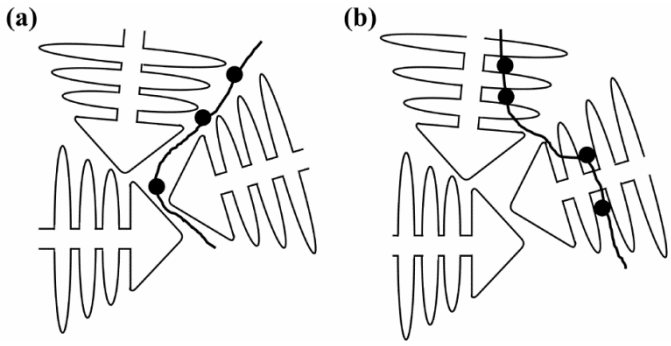

Figure 15 Schematic illustration of the crack (bold lines) linkage process for the (a) intergranular and (b) transgranular fracture modes.

The fatigue life of $0.7P_0$ is longer despite the low-energy intergranular fracture mode. This is because L-PBF parts contain a high density of differently oriented grains [51]. They are formed due to local grain nucleation and competitive grain growth at the solid-liquid interface of the melt pool, where grains with less favourable orientation relative to the temperature gradient stop growing upon encountering the melt pool boundary [60]. The grain

boundaries act as obstacles to dislocation movement and the crack length is longer in the case of intergranular fracture. This explains the richer morphology of the fracture surface of $0.7P_0$ shown in Figure 13 (b). Moreover, as similar factors, i.e. small dendrite size and intergranular fracture, could have been responsible for the higher ductility and longer fatigue life of $0.7P_0$, the direct relationship between ductility and fatigue life could be explained.

C. Special Case – Porosity-driven Crack Initiation for $0.7P_0$

Of the three $0.7P_0$ samples tested at 438 MPa, only one failed by the intergranular path. The rest failed due to porosity-driven crack initiation. As shown in Figure 16 (a), crack originated at a large lack of fusion defect that intercepted the sample surface. Pores of this size are rare in $0.7P_0$ and were only detected by the XCT. In such cases, no intergranular failure was found at the crack origin. Agreeing with the metallographic observation in Figure 4 (a), the lack of fusion defect in $0.7P_0$ was accompanied by an un-melted powder, as shown in Figure 16 (b).

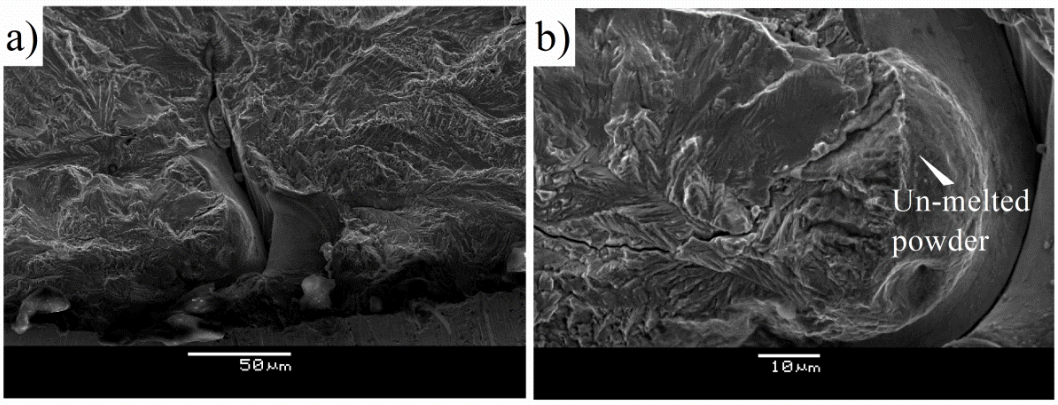

Figure 16 SEM images of fracture surface of $0.7P_0$ subjected to a maximum cyclic stress of 438 MPa. (a) Crack initiation from a lack of fusion defect that intercepts the sample surface, and (b) the enlarged view of (a) showing sintered powder adjacent to the pore.

The fatigue life of the $0.7P_0$ samples are similar regardless of the fracture modes. Two questions arise from this result: (1) why does $0.7P_0$ sustain longer fatigue life than P_0 and $1.3P_0$ despite the porosity-induced cracking, (2) why does porosity-driven failure in $0.7P_0$ produced equivalent fatigue life as the microstructure-driven failure?

With regards to the first question, the effects of finer dendrite cells and particles still apply [61]. For porosity-induced cracking, the crack initiation phase is shortened and the total fatigue life is dominated by crack propagation. Figure 17 (a) shows fatigue crack propagation in a typical L-PBF stainless steel 316L sample. Deflection of crack path, as indicated by the arrows, occurred at the length scale of the grains. A mixture of cleavage ('C') and ductile ('D') fracture modes indicates that grains with different orientations are present; favourably oriented grains failed by cleavage fracture and those oriented to relax the load failed plastically and formed fatigue striations. Crack deflection also occurred at the scale of the dendrite cells, as shown by the arrows in Figure 17 (b).

As lower laser power produces smaller grains and dendrite cells, and a weaker texture in the direction of the temperature gradient during solidification, more significant crack branching should take place in $0.7P_0$. Besides lengthening the crack propagation path, such crack deflections are believed to affect crack growth via the roughness-induced crack closure mechanism [61]. As the applied cyclic stress is low, crack advancement (as shown by the striation marks in Figure 17) is small in comparison with the size of the local microstructure. This, together with the fact that the samples were tested at a small load ratio (R=0.1), makes contact between cracked surfaces likely to occur. When this happens, residual compressive stress in the materials in the wake of the advancing crack reduces the effective stress intensity factor, causing retarded crack growth. The resulting increase in fatigue crack propagation life could have outweighed the reduction due to porosity-driven crack initiation, such that the fatigue life of $0.7P_0$ is still the highest.

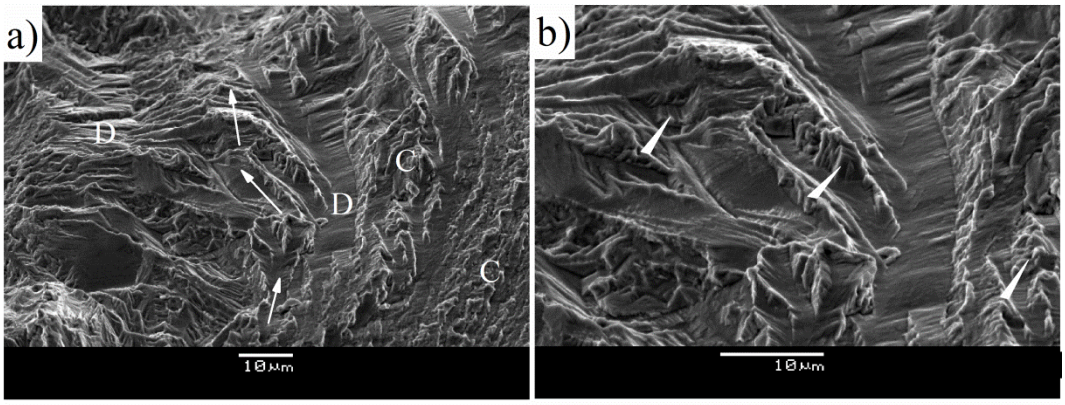

Figure 17 SEM images showing typical crack propagation in laser powder bed fusion stainless steel 316L. (a) Crack deflection occurs at grain level (indicated by arrows) and a mixture of cleavage ('C) and ductile ('D') fracture modes due to differently oriented

grains are present, and (b) crack deflection occurs at sub-grain level (indicated by arrows).

For the second question, several explanations could be possible. Firstly, the pore was not aligned in a favourable orientation for cracking. Secondly, both sides of the pore have a curved shape, which reduced the stress concentrating effect. As the sintered powder is spherical in shape, and the size and texture of the dendrites in the raw powder are different from the bulk material, it could have further reduced the stress concentration at the crack origin and redirected the crack propagation path. However, due to the scattering nature of fatigue test, more samples need to be tested to confirm this result.

3.5 Comparison with Conventional Austenitic Stainless Steel

Different fatigue properties between conventional and L-PBF stainless steel 316L are expected due to the different microstructure and porosity content. Fatigue initiation of conventional coarse grain stainless steel 316L is driven by cyclic slip localisation [62]; for L-PBF parts, the solidification microstructure promotes intergranular crack initiation and crack branching. Second phase particles in stainless steel 316L are rare due to its single phase austenitic structure. However, in L-PBF parts, pores and nano-inclusions are present. This section compares and correlates the high cycle fatigue properties of conventional and L-PBF processed stainless steel 316L.

Figure 18 shows the Gumbel distribution parameters of the L-PBF samples and conventional materials including cast iron [63], alloy steel [64, 65] and carbon steel [64, 66] as collected by Beretta *et al.* [33]. With the exception of $0.5P_0$, L-PBF defects are in general smaller than casting defects. They also have a narrower size distribution, as indicated by the small δ values. This is because localised heating during L-PBF processing produces pores with relatively homogenous size. Comparing with alloy steels, pores in L-PBF samples are larger. Only $1.3P_0$ falls within the parameter range of conventional alloys steels.

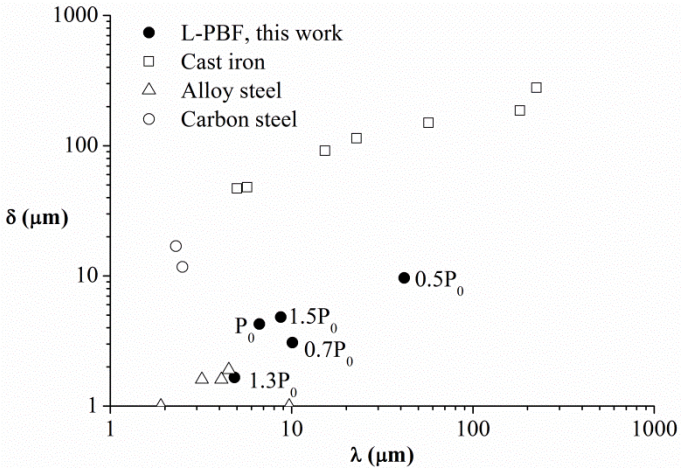

Figure 18 Comparing the Gumbel Extreme Value Distribution parameters of laser powder bed fusion stainless steel 316L with conventional materials.

In terms of the monotonic tensile strength, L-PBF materials have significantly higher strength than the wrought form (ultimate tensile strength: 520-680 MPa; yield strength: 220-270 MPa [17]) due to the ultrafine grains. Even the $0.5P_0$ setting produced similar ultimate tensile strength as the wrought counterpart despite the large amount of porosity. The yield strength to ultimate tensile strength ratios of the samples are all above 0.8. However, the ductility of L-PBF materials is generally lower than the wrought form (elongation to failure: 40-45% [17]). Only $0.7P_0$ and P_0 produced comparable ductility.

Figure 19 compares the high cycle S-N data obtained from this study with 1) the conventional austenitic stainless steel by means of the mean-data curve derived from the ANL (Argonne National Laboratory) fatigue life model [67] and 2) the ASME Code fatigue design curve [68]. The mean curve was obtained from strain-controlled tests of small polished specimen of wrought and cast austenitic stainless steel conducted at room temperature in air under fully reversed loading (R=-1). The ASME Code fatigue design curve defines the allowable number of cycles for a structural material as a function of the applied stress amplitude and was obtained by making adjustments to the mean-data curve to account for factors such as material variability, data scatter, surface finish, specimen size, etc. To make results obtained at different load ratios comparable, the Goodman relationship was used to adjust the data obtained in this work for plotting Figure 19.

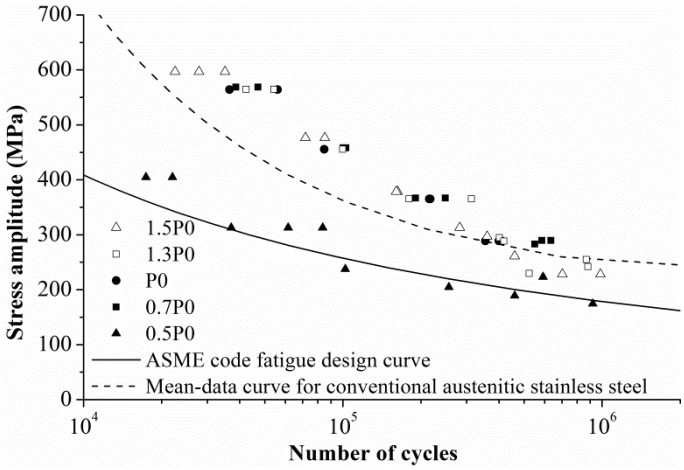

Figure 19 Comparing S-N data of laser powder bed fusion stainless steel 316L from this work with conventional austenitic stainless steel at *R*=-1. Experiments in this work were conducted at *R*=0.1, so results had been converted to *R*=-1 using the Goodman equation.

With the exception of $0.5P_0$, L-PBF stainless steel 316L shows equivalent if not superior fatigue properties to conventional austenitic stainless steel. The ASME fatigue design curve is still applicable for providing a conservative estimate for the fatigue strength of near fully dense L-PBF materials. However, in the shorter life region, it could be too conservative such that the advantage of high strength offered by L-PBF processing cannot be exploited.

Data from this work intersect the mean curve at about 300 MPa. This corresponds to the yield strength of the conventional material. The high yield strength allows L-PBF materials to withstand higher cyclic stress without undergoing plastic deformation. Below the intersection point, the fatigue strength of L-PBF parts is comparable with the conventional material. The data points for $1.3P_0$ and $1.5P_0$ however, are below the mean curve. As their ductility values are slightly inferior to that of the conventional form, this result is in good agreement with the trend observed in this work, where ductility varies directly with fatigue resistance in the low stress high cycle fatigue regime. For L-PBF parts, ductility is constrained by the effects of porosity and solidification microstructure on fracture.

The poor fatigue strength of $0.5P_0$ is clearly a result of process-induced porosity, as its pore sizes are far beyond the range of the conventional alloy steels. Nonetheless, a small amount of porosity, as in the cases of $0.7P_0$ and $1.5P_0$, is tolerable as long as it does not impinge greatly on the material strength and ductility.

4. Conclusions

The following conclusions can be drawn with regards to the influence of processing parameter on the high cycle fatigue properties of L-PBF stainless steel 316L:

1) For horizontally-oriented stainless steel 316L samples, the safe processing region is within ±30% E_{d0}, where near fully dense parts with minimal cracks and optimum fatigue S-N properties can be produced. Beyond this region, both over-melting and under-melting produce parts with critical porosities that trigger premature crack initiation.

2) Within the safe processing region, high cycle fatigue properties are not sensitive to porosity due to fatigue crack initiation from slip planes in dendrite cells or grain boundary particles. Processing strategies that increase the cooling rate during solidification, e.g. lower laser power, can improve fatigue resistance in the longer life regime, possibly by promoting intergranular fatigue crack initiation and crack branching.

3) Regardless of the processing condition and porosity level, fatigue strength correlates directly with ductility and tensile strength in the longer and shorter fatigue life regimes respectively. In the former case, similar factors, such as the size of the dendrite cells and grain boundary particles, that govern the ductility and high cycle fatigue fracture mechanisms could be responsible for the direct relationship. Based on these relationships, the difference in the high cycle fatigue properties of L-PBF and conventional stainless steel 316L can be explained.

4) From the stand point of design engineering, samples could be built at several different processing parameters and tested under monotonic tensile loading first. Appropriate processing conditions could be selected depending on the service load of the component, e.g. processing condition that generates the highest ductility should be used for fabricating parts for low cyclic stress applications.

Acknowledgement

This work was supported by the Singapore Economic Development Board (EDB) Industrial Postgraduate Programme (IPP).

References

[1] R. Li, J. Liu, Y. Shi, L. Wang, W. Jiang, Balling behavior of stainless steel and nickel powder during selective laser melting process, Int. J. Adv. Manuf. Technol. 59(9-12) (2012) 1025-1035.

[2] D. Gu, Y. Shen, Balling phenomena in direct laser sintering of stainless steel powder: metallurgical mechanisms and control methods, Mater. Des. 30(8) (2009) 2903-2910.

[3] W.E. King, H.D. Barth, V.M. Castillo, G.F. Gallegos, J.W. Gibbs, D.E. Hahn, C. Kamath, A.M. Rubenchik, Observation of keyhole-mode laser melting in laser powder-bed fusion additive manufacturing, J. Mater. Process. Technol. 214(12) (2014) 2915-2925.

[4] Y. Liu, Y. Yang, S. Mai, D. Wang, C. Song, Investigation into spatter behavior during selective laser melting of AISI 316L stainless steel powder, Mater. Des. 87 (2015) 797-806.

[5] S. Siddique, M. Imran, M. Rauer, M. Kaloudis, E. Wycisk, C. Emmelmann, F. Walther, Computed tomography for characterization of fatigue performance of selective laser melted parts, Mater. Des. 83 (2015) 661-669.

[6] M. Akita, Y. Uematsu, T. Kakiuchi, M. Nakajima, R. Kawaguchi, Defect-dominated fatigue behavior in type 630 stainless steel fabricated by selective laser melting, Mater. Sci. Eng., A 666 (2016) 19-26.

[7] H. Gong, K. Rafi, T. Starr, B. Stucker, Effect of defects on fatigue tests of as-built Ti-6Al-4V parts fabricated by selective laser melting, Solid freeform fabrication symposium, University of Texas Austin, Texas, 2012, pp. 499-506.

[8] E. Wycisk, A. Solbach, S. Siddique, D. Herzog, F. Walther, C. Emmelmann, Effects of defects in laser additive manufactured Ti-6Al-4V on fatigue properties, Physics Procedia 56 (2014) 371-378.

[9] A. Yadollahi, N. Shamsaei, S.M. Thompson, A. Elwany, L. Bian, Effects of building orientation and heat treatment on fatigue behavior of selective laser melted 17-4 PH stainless steel, Int. J. Fatigue 94 (2017) 218-235.

[10] R. Shrestha, J. Simsiriwong, N. Shamsaei, S.M. Thompson, L. Bian, Effect of build orientation on the fatigue behavior of stainless steel 316l manufactured via a laser-powder bed fusion process.

[11] E. Brandl, U. Heckenberger, V. Holzinger, D. Buchbinder, Additive manufactured AlSi10Mg samples using Selective Laser Melting (SLM): Microstructure, high cycle fatigue, and fracture behavior, Mater. Des. 34 (2012) 159-169.
[12] S. Leuders, M. Thöne, A. Riemer, T. Niendorf, T. Tröster, H.A. Richard, H.J. Maier, On the mechanical behaviour of titanium alloy TiAl6V4 manufactured by selective laser melting: Fatigue resistance and crack growth performance, Int. J. Fatigue 48 (2013) 300-307.
[13] K. Saeidi, X. Gao, Y. Zhong, Z.J. Shen, Hardened austenite steel with columnar sub-grain structure formed by laser melting, Mater. Sci. Eng., A 625 (2015) 221-229.
[14] Y. Zhong, L. Liu, S. Wikman, D. Cui, Z. Shen, Intragranular cellular segregation network structure strengthening 316L stainless steel prepared by selective laser melting, J. Nucl. Mater. 470 (2016) 170-178.
[15] Q. Wang, Microstructural effects on the tensile and fracture behavior of aluminum casting alloys A356/357, Metall. Mater. Trans. A 34(12) (2003) 2887-2899.
[16] C. Cáceres, Q. Wang, Dendrite cell size and ductility of Al—Si—Mg casting alloys: Spear and Gardner revisited, International Journal of Cast Metals Research 9(3) (1996) 157-162.
[17] I. Tolosa, F. Garciandía, F. Zubiri, F. Zapirain, A. Esnaola, Study of mechanical properties of AISI 316 stainless steel processed by "selective laser melting", following different manufacturing strategies, Int. J. Adv. Manuf. Technol. 51(5-8) (2010) 639-647.
[18] I. Altenberger, B. Scholtes, U. Martin, H. Oettel, Cyclic deformation and near surface microstructures of shot peened or deep rolled austenitic stainless steel AISI 304, Mater. Sci. Eng., A 264(1) (1999) 1-16.
[19] Y. Furuya, S. Matsuoka, S. Shimakura, T. Hanamura, S. Torizuka, Fatigue strength of ultrafine ferrite-cementite steels and effects of strengthening mechanisms, Metall. Mater. Trans. A 38(12) (2007) 2984-2991.
[20] A. Hamada, L. Karjalainen, High-cycle fatigue behavior of ultrafine-grained austenitic stainless and TWIP steels, Mater. Sci. Eng., A 527(21) (2010) 5715-5722.
[21] T.M. Mower, M.J. Long, Mechanical behavior of additive manufactured, powder-bed laser-fused materials, Mater. Sci. Eng., A 651 (2016) 198-213.
[22] J. Haan, M. Asseln, M. Zivcec, J. Eschweiler, R. Radermacher, C. Broeckmann, Effect of subsequent Hot Isostatic Pressing on mechanical properties of ASTM F75 alloy produced by Selective Laser Melting, Powder Metall. 58(3) (2015) 161-165.

[23] A. Riemer, S. Leuders, M. Thöne, H. Richard, T. Tröster, T. Niendorf, On the fatigue crack growth behavior in 316L stainless steel manufactured by selective laser melting, Eng. Fract. Mech. 120 (2014) 15-25.
[24] S. Leuders, T. Lieneke, S. Lammers, T. Tröster, T. Niendorf, On the fatigue properties of metals manufactured by selective laser melting–The role of ductility, J. Mater. Res. 29(17) (2014) 1911-1919.
[25] M.L. Pace, A. Guarnaccio, P. Dolce, D. Mollica, G.P. Parisi, A. Lettino, L. Medici, V. Summa, R. Ciancio, A. Santagata, 3D additive manufactured 316L components microstructural features and changes induced by working life cycles, Appl. Surf. Sci. 418, Part B (2017) 437-445.
[26] P. Ganesh, R. Kaul, G. Sasikala, H. Kumar, S. Venugopal, P. Tiwari, S. Rai, R. Prasad, L. Kukreja, Fatigue crack propagation and fracture toughness of laser rapid manufactured structures of AISI 316L stainless steel, Metallography, Microstructure, and Analysis 1(3) (2014) 36-45.
[27] R. Li, J. Liu, Y. Shi, M. Du, Z. Xie, 316L Stainless Steel with Gradient Porosity Fabricated by Selective Laser Melting, J. Mater. Eng. Perform. 19(5) (2010) 666-671.
[28] M.M. Dewidar, K.A. Khalil, J.K. Lim, Processing and mechanical properties of porous 316L stainless steel for biomedical applications, Transactions of Nonferrous Metals Society of China 17(3) (2007) 468-473.
[29] B. Vrancken, Study of Residual Stresses in Selective Laser Melting, (2016).
[30] A. Spierings, M. Schneider, R. Eggenberger, Comparison of density measurement techniques for additive manufactured metallic parts, Rapid Prototyping Journal 17(5) (2011) 380-386.
[31] W. King, A. Anderson, R. Ferencz, N. Hodge, C. Kamath, S. Khairallah, A. Rubenchik, Laser powder bed fusion additive manufacturing of metals; physics, computational, and materials challenges, Appl. Phys. Rev. 2(4) (2015) 041304.
[32] Y. Murakami, S. Beretta, Small defects and inhomogeneities in fatigue strength: experiments, models and statistical implications, Extremes 2(2) (1999) 123-147.
[33] S. Beretta, Y. Murakami, Statistical analysis of defects for fatigue strength prediction and quality control of materials, Fatigue Fract. Eng. Mater. Struct. 21(9) (1998) 1049-1065.
[34] F. Ghanem, H. Sidhom, C. Braham, M. Fitzpatrick, Effect of near-surface residual stress and microstructure modification from machining on the fatigue endurance of a tool steel, J. Mater. Eng. Perform. 11(6) (2002) 631-639.

[35] C. Kamath, B. El-dasher, G.F. Gallegos, W.E. King, A. Sisto, Density of additively-manufactured, 316L SS parts using laser powder-bed fusion at powers up to 400 W, Int. J. Adv. Manuf. Technol. 74(1-4) (2014) 65-78.
[36] B. Zhang, L. Dembinski, C. Coddet, The study of the laser parameters and environment variables effect on mechanical properties of high compact parts elaborated by selective laser melting 316L powder, Mater. Sci. Eng., A 584 (2013) 21-31.
[37] S. Dadbakhsh, L. Hao, N. Sewell, Effect of selective laser melting layout on the quality of stainless steel parts, Rapid Prototyping Journal 18(3) (2012) 241-249.
[38] J. Cherry, H. Davies, S. Mehmood, N. Lavery, S. Brown, J. Sienz, Investigation into the effect of process parameters on microstructural and physical properties of 316L stainless steel parts by selective laser melting, Int. J. Adv. Manuf. Technol. 76(5-8) (2015) 869-879.
[39] A. Spierings, G. Levy, Comparison of density of stainless steel 316L parts produced with selective laser melting using different powder grades, Proceedings of the Annual International Solid Freeform Fabrication Symposium, Austin, TX, 2009, pp. 342-353.
[40] Z. Sun, X. Tan, S.B. Tor, W.Y. Yeong, Selective laser melting of stainless steel 316L with low porosity and high build rates, Mater. Des. 104 (2016) 197-204.
[41] C.Y. Yap, C.K. Chua, Z.L. Dong, An effective analytical model of selective laser melting, Virtual and Physical Prototyping 11(1) (2016) 21-26.
[42] V. Shankar, T.P.S. Gill, S.L. Mannan, S. Sundaresan, Solidification cracking in austenitic stainless steel welds, Sadhana 28(3) (2003) 359-382.
[43] Y. Li, D. Gu, Parametric analysis of thermal behavior during selective laser melting additive manufacturing of aluminum alloy powder, Mater. Des. 63 (2014) 856-867.
[44] B. Song, X. Zhao, S. Li, C. Han, Q. Wei, S. Wen, J. Liu, Y. Shi, Differences in microstructure and properties between selective laser melting and traditional manufacturing for fabrication of metal parts: A review, Frontiers of Mechanical Engineering 10(2) (2015) 111-125.
[45] G. Kasperovich, J. Haubrich, J. Gussone, G. Requena, Correlation between porosity and processing parameters in TiAl6V4 produced by selective laser melting, Mater. Des. 105 (2016) 160-170.
[46] M. Simonelli, C. Tuck, N.T. Aboulkhair, I. Maskery, I. Ashcroft, R.D. Wildman, R. Hague, A study on the laser spatter and the oxidation reactions during selective laser melting of 316L stainless steel, Al-Si10-Mg, and Ti-6Al-4V, Metall. Mater. Trans. A 46(9) (2015) 3842-3851.

[47] K. Darvish, Z.W. Chen, T. Pasang, Reducing lack of fusion during selective laser melting of CoCrMo alloy: Effect of laser power on geometrical features of tracks, Mater. Des. 112 (2016) 357-366.
[48] E. Zhang, B. Wang, On the compressive behaviour of sintered porous coppers with low to medium porosities—Part I: Experimental study, International Journal of Mechanical Sciences 47(4) (2005) 744-756.
[49] A.L. Gurson, Continuum Theory of Ductile Rupture by Void Nucleation and Growth: Part I—Yield Criteria and Flow Rules for Porous Ductile Media, J. Eng. Mater. Technol. 99(1) (1977) 2-15.
[50] R. Hardin, C. Beckermann, Effect of porosity on deformation, damage, and fracture of cast steel, Metall. Mater. Trans. A 44(12) (2013) 5316-5332.
[51] D. Wang, C. Song, Y. Yang, Y. Bai, Investigation of crystal growth mechanism during selective laser melting and mechanical property characterization of 316L stainless steel parts, Mater. Des. 100 (2016) 291-299.
[52] R. Amano, Z. Xu, J.M. Lucci, P. Rohatgi, A Numerical Study of a Cooling Ratio for Laser Based Prototyping Technology with a Sample of 316l Stainless Steel, Open Automation and Control Systems Journal 4 (2012) 1-7.
[53] N. Klingbeil, S. Bontha, C. Brown, D. Gaddam, P. Kobryn, H. Fraser, J. Sears, Effects of process variables and size scale on solidification microstructure in laser-based solid freeform fabrication of Ti-6Al-4V, WRIGHT STATE UNIV DAYTON OH, 2004.
[54] C.H. Caceres, J.R. Griffiths, Damage by the cracking of silicon particles in an Al-7Si-0.4Mg casting alloy, Acta Mater. 44(1) (1996) 25-33.
[55] ASM Handbook, Volume 1: Properties and Selection: Irons, Steels, and High-Performance Alloys, ASM International, 1990, p. 1063.
[56] K. Obrtlík, J. Polák, M. Hájek, A. Vašek, Short fatigue crack behaviour in 316L stainless steel, Int. J. Fatigue 19(6) (1997) 471-475.
[57] D.L. Olson, R. Dixon, A.L. Liby, Welding: theory and practice, Elsevier2012.
[58] J. Major, Porosity control and fatigue behavior in A356-T61 aluminum alloy, Transactions-American Foundrymens Society (1998) 901-906.
[59] M.I. Houria, Y. Nadot, R. Fathallah, M. Roy, D.M. Maijer, Influence of casting defect and SDAS on the multiaxial fatigue behaviour of A356-T6 alloy including mean stress effect, Int. J. Fatigue 80 (2015) 90-102.

[60] A.R.A. Dezfoli, W.-S. Hwang, W.-C. Huang, T.-W. Tsai, Determination and controlling of grain structure of metals after laser incidence: Theoretical approach, Scientific Reports 7 (2017) 41527.
[61] S. Kumai, J. Hu, Y. Higo, S. Nunomura, Effects of dendrite cell size and particle distribution on the near-threshold fatigue crack growth behaviour of cast Al SiCp composites, Acta Mater. 44(6) (1996) 2249-2257.
[62] A. Weidner, J. Man, W. Skrotzki, J. Polák, Slip localization and dislocation structure at early stages of fatigue damage in austenitic stainless steel (316L), ICF12, Ottawa 2009, 2013.
[63] M. Endo, X.-B. Wang, Effects of Graphite and Artificial Small Defect on the Fatigue Strength of Current Ductile Cast Irons, Journal of the Society of Materials Science, Japan 43(493) (1994) 1245-1250.
[64] Y. Murakami, Effects of small defects and nonmetallic inclusions on the fatigue strength of metals, JSME international journal. Ser. 1, Solid mechanics, strength of materials 32(2) (1989) 167-180.
[65] Y. Murakami, T. Toriyama, E. Coudert, Instructions for a new method of inclusion rating and correlations with the fatigue limit, J. Test. Eval. 22(4) (1994) 318-326.
[66] Y. Murakami, M. Takada, T. Toriyama, Super-long life tension–compression fatigue properties of quenched and tempered 0.46% carbon steel, Int. J. Fatigue 20(9) (1998) 661-667.
[67] O.K. Chopra, W.J. Shack, The effect of lwr coolant environments on the fatigue life of reactor materials, ASME 2006 Pressure Vessels and Piping/ICPVT-11 Conference, American Society of Mechanical Engineers, 2006, pp. 191-204.
[68] ASME, ASME Boiler and Pressure Vessel Code VIII Div 2 2010.